

# Interactive Simulation of Needle Insertion Models

Simon P. DiMaio\*, Member, IEEE, and Septimiu E. Salcudean, Fellow, IEEE

**Abstract**—A novel interactive virtual needle insertion simulation is presented. The simulation models are based on measured planar tissue deformations and needle insertion forces. Since the force-displacement relationship is only of interest along the needle shaft, a condensation technique is shown to reduce the computational complexity of linear simulation models significantly. As the needle penetrates or is withdrawn from the tissue model, the boundary conditions that determine the tissue and needle motion change. Boundary condition and local material coordinate changes are facilitated by fast low-rank matrix updates. A large-strain elastic needle model is coupled to the tissue models to account for needle deflection and bending during simulated insertion. A haptic environment, based on these novel interactive simulation techniques, allows users to manipulate a three-degree-of-freedom virtual needle as it penetrates virtual tissue models, while experiencing steering torques and lateral needle forces through a planar haptic interface.

**Index Terms**—Finite-element method, flexible needle, haptics, needle deflection, needle insertion model, percutaneous intervention, surgical simulation, tissue model, training.

## I. INTRODUCTION

SOME of the most common procedures encountered in modern clinical practice involve the percutaneous insertion of needles and catheters. Such procedures range in complexity from superficial needle sticks to the biopsy of deep-seated tumors, and involve subcutaneous insertions of long, slender surgical tools and needles into soft, inhomogeneous tissue, usually with limited visual feedback from below the skin's surface. Physicians and surgeons often rely on kinesthetic feedback from the tool, correlated with their own mental three-dimensional (3-D) visualization of anatomic structures.

Complications arising from the complexity of such interventions have been studied in biopsy [1], [2], brachytherapy [3] and particularly in anaesthesia [4]–[8], where it is found that such complications are due, in large part, to poor technique and needle placement [4]. Although the incidence of such complications is on the order of only a few percent [4], [6], [7], their effects can be significant, long-lasting and even fatal [9]. Percutaneous procedures involving needle insertions include vaccinations, blood/fluid sampling, regional anaesthesia, tissue biopsy, abscess drainage, catheter insertion, cryogenic ablation, electrolytic ablation, brachytherapy, neurosurgery, deep brain stim-

ulation and minimally invasive surgeries, to name but a few. Medical students and residents typically learn such procedures by performing them on real patients, under close supervision. For example, it is estimated that between 45 and 90 attempts are required to become proficient in some epidural and spinal procedures, and an even larger number of attempts may be required for peripheral nerve blocks that have less well-defined tactile queues [8]. While mannequins, cadavers and animal models do exist for training, they are often unrealistic or are ethically questionable.

Virtual-reality-based training systems for catheter insertion [10]–[12], endoscopy [13], epidural lumbar puncture [5], [14]–[21], spine biopsy [22], breast biopsy [1], neurosurgical probe insertion [23], interstitial brachytherapy [24], prostate needle biopsy [25], etc. constitute part of the present trend toward computer-based simulators for medical and surgical training [26], [27]. Experienced physicians and surgeons are also taking advantage of these developments by using simulators to plan and to rehearse complex procedures, to predict the outcomes of procedures, to design and evaluate new methods and equipment [28], [29], and to control complex medical robotic systems [30]–[32]. The majority of the simulation and manipulation systems for needle- and catheter-based procedures have been built using largely phenomenological and heuristic models that have not been validated, and that are not generalizable. In some cases, lookup tables—based on empirical values—determine needle force feedback versus depth for 1-DOF interaction [11], [16]. Others employ elastic, viscous and viscoelastic models to approximate needle driving impedance along the axial direction [14], [15]. Recent important work has been undertaken to better characterize needle-tissue interaction [33]–[35]; however, needle-tissue contact forces, soft tissue interaction, deformation and needle flexibility have not been considered together in prior work.

In previous work, we described a method for estimating needle shaft forces that occur during insertions into tissue phantoms, based on empirical results [36], [37]. We showed that the estimated needle shaft force distribution could be applied to a numerical tissue model for a physically based simulation of needle insertion. An overview of the approach to interactive simulation of these models was also given. In this paper, simulations of multidegree-of-freedom trajectories of flexible needles in elastic tissue models are described in detail. Interactive training systems require model update rates that match human sensory perception at visually and kinesthetically convincing rates on the order of 30 Hz and 500 Hz, respectively. In Sections II–VIII we describe a needle insertion simulation algorithm that can be computed at visually interactive rates, while in Section IX we extend fast numerical techniques for simulating reasonably complex models at “haptic” rates.

Manuscript received November 11, 2003; revised January 2, 2005. Asterisk indicates corresponding author.

\*S. P. DiMaio was with the Department of Electrical and Computer Engineering, 2356 Main Mall, Vancouver, BC V6T 1Z4, Canada (e-mail: simond@ece.ubc.ca). He is now with the Surgical Planning Laboratory, Harvard Medical School, Department of Radiology, L1-050, Brigham and Women's Hospital, 75 Francis Street, Boston, MA 02115 USA (e-mail: simond@bwh.harvard.edu).

S. E. Salcudean is with the Department of Electrical and Computer Engineering, the University of British Columbia, 2356 Main Mall, Vancouver, BC V6T 1Z4, Canada (e-mail: tims@ece.ubc.ca).

Digital Object Identifier 10.1109/TBME.2005.847548

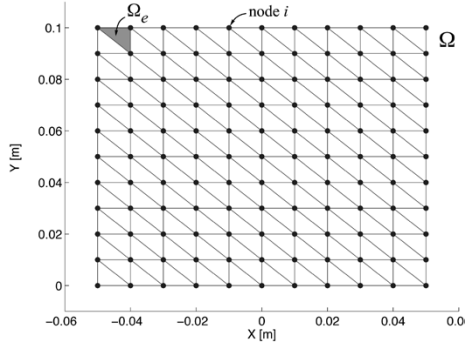


Fig. 1. The continuous domain  $\Omega$  is divided into a finite number of discrete elements  $\Omega_e$  by a mesh of nodes.

The paper is organized as follows. Section II reviews the material and force models that form the basis of the needle insertion simulation. Sections III and IV discuss matrix condensation and low-rank boundary condition updates that help to reduce the computational complexity of these models. Section V addresses meshing issues, while Section VI describes a low-rank scheme for updating material coordinate frames at tissue mesh nodes. Sections VII and VIII describe a flexible needle model, and its coupling with the tissue model. The implementation of an interactive haptic needle insertion environment is detailed in Section IX. Finally, Sections X, XI, and XII discuss limitations, conclusions and plans for future work.

## II. MATERIAL AND FORCE MODELS

Tissue deformation is complex and is still the subject of much research ([38]–[40] and many others). In general, tissue is inhomogeneous and exhibits nonlinear, anisotropic elastic and viscous behavior; therefore, models are quite complex. As a first approximation, this study focuses on linear elastostatic models that predict elastic tissue deformations in two dimensions. Such models are characterized by two parameters, namely *Young's Modulus* and the *Poisson Ratio*, which are shown to be identified from experiments with tissue phantoms in [36]. For linear elastic materials, the generalized Hooke's Law states that

$$\boldsymbol{\sigma} = C\boldsymbol{\epsilon} \quad (1)$$

where  $C$  is a constant *material matrix*, and  $\boldsymbol{\sigma}$  and  $\boldsymbol{\epsilon}$  are stress and strain vectors, respectively. The total strain energy over a solid elastic body  $\Omega$  is expressed as follows:

$$E_{\text{strain}} = \frac{1}{2} \int_{\Omega} \boldsymbol{\epsilon}^T(x) \boldsymbol{\sigma}(x) dx. \quad (2)$$

The relationship between applied force and material deformation is derived by discretising this integral using Finite Element Analysis. A rectangular block of elastic material is discretised as shown in Fig. 1. Each element  $e$  reaches its static equilibrium state when the first variation of the energy functional  $\delta E^e$  vanishes, where  $E^e$  is the energy of a single element  $e$  under load. This is expressed as follows:

$$\delta E^e = \int_{\Omega^e} A^e \underline{\mathbf{u}}^e dx - \underline{\mathbf{f}}^e = 0 \quad (3)$$

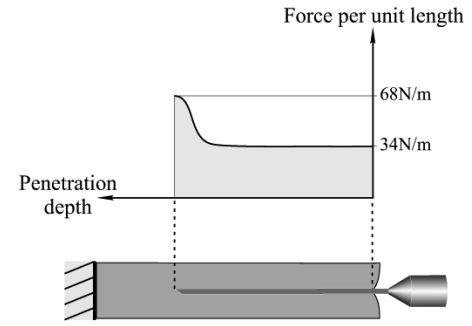


Fig. 2. Estimated needle force distribution for a 1 mm/s insertion.

where the  $A^e$  matrix characterizes the elastic behavior of element  $\Omega^e$ , and  $\underline{\mathbf{u}}^e$  and  $\underline{\mathbf{f}}^e$  are displacement and force vectors for those mesh nodes that constitute element  $e$  [41]. Over the entire set of nodes on body  $\Omega$ , this leads to a set of  $2n$  linear equations

$$\begin{aligned} \mathbf{K}_{(2n \times 2n)} \underline{\mathbf{u}} &= \underline{\mathbf{f}} \\ \Rightarrow \underline{\mathbf{u}} &= \mathbf{K}^{-1} \underline{\mathbf{f}} \end{aligned} \quad (4)$$

as shown in [37].

Needle force distributions for homogeneous and layered-inhomogeneous tissue phantoms, over a range of insertion velocities, are provided in [36] and [37], and are used as boundary values for insertion simulation. An example of a force distribution found to occur along the needle shaft during insertion into a soft tissue phantom at a velocity of 1 mm/s, is illustrated in Fig. 2.

The needle insertion simulation is based on the simple algorithm summarized in [36]. The algorithm is not suitable for general trajectories because:

- 1) the needle shaft might not always intercept control points or nodes on the discretised tissue model;
- 2) there is no contact model;
- 3) the needle may not move in a straight line or with uniform velocity;
- 4) the needle may bend in practice.

Each of these issues, as well as real-time model computation are considered in this paper, culminating in a new general algorithm that is described by the flowchart in Fig. 22.

## III. CONDENSING THE NUMERICAL SYSTEM

The behavior of a continuum model that is discretised by the *finite-element method* is observed through the behavior of a finite set of mesh nodes. Real-time computation of the needle insertion model is complicated by the “curse of dimensionality” that is established by the large number of linear equations required to describe even small models. For example, a  $10 \times 10$  node two-dimensional (2-D) model, discretised as shown in Fig. 1, results in 200 linear equations, and a system matrix  $\mathbf{K}$  containing 40 000 elements. For a  $30 \times 30$  node discretization, the number of matrix elements swells to 3.24 million, while a  $10 \times 10 \times 10$  node 3-D block results in 3000 linear equations in as many unknowns (9 million matrix elements). It is clearly infeasible to solve such systems at haptic sample rates of 500 Hz and higher. For large volumes of tissue that are

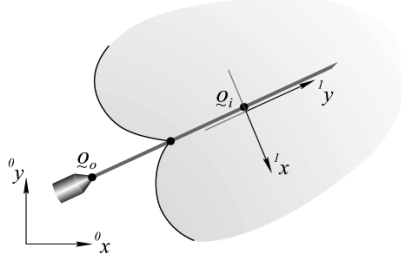


Fig. 3. Mesh nodes lying along the needle are constrained along the  $^1x$ -axis, and either *slip* or *stick* along the  $^1y$ -axis. Point  $\tilde{q}_i$  represents a tissue mesh node that is coincident with the needle shaft, while  $\tilde{q}_o$  indicates the needle base.

finely discretised, the size of matrix  $\mathbf{K}$  in (4) becomes large due to the large number of material nodes at which force or displacement need to be computed. For needle insertion simulation it is not necessary to consider the motion of nodes that are not visible (e.g., interior nodes), or the forces applied at nodes that are not in direct contact with the needle shaft. It is evident that the large majority of mesh nodes are neither visible nor palpable; therefore, the system of linear equations (4) can be reduced to

$$\underline{\mathbf{u}}_{\mathcal{W}} = \mathbf{K}_{\mathcal{W}}^{-1} \underline{\mathbf{f}}_{\mathcal{W}} \quad (5)$$

where only the behavior at a small subset  $\mathcal{W}$  of mesh nodes (called *working nodes*) is explicitly considered. These are the tissue nodes that are in contact with the needle. At run-time, the subset of working nodes  $\mathcal{W}$  is selected and the system matrix is reduced to  $\mathbf{K}_{\mathcal{W}}^{-1}$ . As the needle penetrates the tissue surface, it intercepts hidden nodes that need to be re-introduced into the reduced system by simply adding new matrix rows and columns to  $\mathbf{K}_{\mathcal{W}}^{-1}$  from  $\mathbf{K}^{-1}$ , which is precomputed (new node intercepts are detected in box 1 of Fig. 22). The matrix reduction approach is similar to the condensation techniques discussed in [42], and the *Boundary Element Method* selected by [38]; however, in this paper access to the interior of the tissue volumes is retained for quick inclusion when needle penetration occurs.

Most tissue model nodes that are not in  $\mathcal{W}$  (i.e., that are eliminated during condensation) are traction nodes that require a zero force boundary constraint. Therefore, it is convenient to work with  $\mathbf{K}^{-1}$ , rather than  $\mathbf{K}$ . Prior to simulation, the entire stiffness matrix  $\mathbf{K}$  is inverted and stored as  $(\mathbf{K}^{-1})_0$ . The condensed *working matrix*  $\mathbf{K}_{\mathcal{W}}^{-1}$  is dynamically constituted from the rows and columns of  $(\mathbf{K}^{-1})_0$ , as required during simulation (i.e., when a node is added).

#### IV. CONTACT MODEL AND LOW RANK BOUNDARY CONDITION UPDATES

Mesh nodes on the tissue model that are in contact with the needle are constrained as shown in Fig. 3. If the needle is rigid, then the lateral position of the node is fixed along the  $^1x$ -axis, constituting a *displacement boundary condition*. Along the needle shaft, the node force or node displacement may be constrained, depending on its state of contact with the needle (i.e., sticking to the needle, or slipping) [43]. If the node

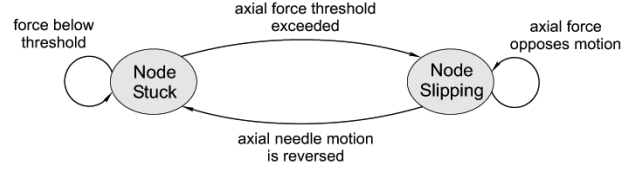


Fig. 4. A finite state automaton for stick-slip contact between tissue mesh nodes and the needle. Such an automaton governs the contact behavior at each needle node.

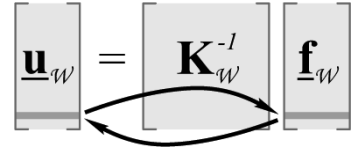


Fig. 5. A boundary condition change at a contact node involves the exchange of displacement and force variables between the left- and right-hand sides of the tissue model equations.

is free to slide along the needle shaft, then a *force boundary condition* is applied along the  $^1y$ -axis, and a constant force consistent with the force distribution (e.g., see Fig. 2) is applied to the slipping node. If it is in the *stuck* state, then the node is constrained to lie at a fixed point on the needle, namely along the  $^1y$  axis (contact states are checked in box 4 of Fig. 22).

The physical contact behavior between needle and tissue is not known; therefore, a stick-slip model is adopted in order to be able to apply a needle force profile consistent with that determined experimentally. A finite-state automaton is applied at each contact node (a tissue mesh node that is in contact with the needle) to simulate stick-slip behavior (see Fig. 4). Axial force thresholds are set according to the force distribution (e.g., as shown in Fig. 2), such that the experimentally derived needle shaft forces are applied when simulated needle nodes are in the *slip* state. During simulated insertion, the boundary conditions at contact nodes will change according to their contact state. The system of equations in (5) is rearranged in order to reflect the resulting inhomogeneous collection of boundary conditions

$$\underline{\mathbf{u}}_{\mathcal{W}} = \mathbf{K}_{\mathcal{W}}^{-1} \underline{\mathbf{f}}_{\mathcal{W}} \rightarrow \underline{\mathbf{x}}_{\mathcal{W}} = (\mathbf{K}_{\mathcal{W}}^{-1})' \underline{\mathbf{y}}_{\mathcal{W}} \quad (6)$$

where  $\underline{\mathbf{x}}_{\mathcal{W}}$  and  $\underline{\mathbf{y}}_{\mathcal{W}}$  are formed by exchanging elements between  $\underline{\mathbf{u}}_{\mathcal{W}}$  and  $\underline{\mathbf{f}}_{\mathcal{W}}$ , as illustrated in Fig. 5.

The  $\underline{\mathbf{x}}_{\mathcal{W}}$  vector contains those variables that are to be solved, while  $\underline{\mathbf{y}}_{\mathcal{W}}$  contains parameters (forces and displacements) that are specified as boundary constraints. For example, if a displacement constraint is applied at the  $i$ th node, then the displacement vector  $[u_i^x \ u_i^y]^T$  is specified as a constraint, and the force vector  $[f_i^x \ f_i^y]^T$  is to be solved. The vectors  $\underline{\mathbf{x}}_{\mathcal{W}}$  and  $\underline{\mathbf{y}}_{\mathcal{W}}$  become

$$\begin{aligned} \underline{\mathbf{x}}_{\mathcal{W}} &= [u_1^x \ u_1^y \ u_2^x \ \dots \ f_i^x \ f_i^y \ \dots \ u_n^x \ u_n^y]^T \\ \underline{\mathbf{y}}_{\mathcal{W}} &= [f_1^x \ f_1^y \ f_2^x \ \dots \ u_i^x \ u_i^y \ \dots \ f_n^x \ f_n^y]^T. \end{aligned} \quad (7)$$

Similarly, if a displacement constraint is applied only along the  $^1x$  axis at the  $i$ th node, then the vector  $[u_i^x \ f_i^y]^T$  is known, and  $[f_i^x \ u_i^y]^T$  is to be solved. The vectors  $\underline{\mathbf{x}}_{\mathcal{W}}$  and  $\underline{\mathbf{y}}_{\mathcal{W}}$  become

$$\begin{aligned}\underline{\mathbf{x}}_{\mathcal{W}} &= [u_1^x \ u_1^y \ u_2^x \ \cdots \ f_i^x \ u_i^y \ \cdots \ u_n^x \ u_n^y]^T \\ \underline{\mathbf{y}}_{\mathcal{W}} &= [f_1^x \ f_1^y \ f_2^x \ \cdots \ u_i^x \ f_i^y \ \cdots \ f_n^x \ f_n^y]^T.\end{aligned}\quad (8)$$

A single boundary condition change can be expressed as an inexpensive low-rank update to  $\mathbf{K}_{\mathcal{W}}^{-1}$

$$(\mathbf{K}_{\mathcal{W}}^{-1})' = \mathbf{K}_{\mathcal{W}}^{-1} - \frac{\mathbf{c}_i \cdot \mathbf{r}_i}{p_i} \quad (9)$$

where  $p_i$  is the  $i$ th pivot of  $\mathbf{K}_{\mathcal{W}}^{-1}$ ;  $\mathbf{c}_i$  and  $\mathbf{r}_i$  are the  $i$ th column and  $i$ th row of  $\mathbf{K}_{\mathcal{W}}^{-1}$ , respectively, with the exception of their  $i$ th coordinates, which are set to  $(p_i + 1)$  and  $(p_i - 1)$ , respectively (boundary condition changes occur in boxes 3 and 5 of Fig. 22).  $(\mathbf{K}_{\mathcal{W}}^{-1})'$  is the new system matrix. This approach to boundary condition changes results in an  $O(n^2)$  computation rather than the  $O(n^3)$  operation required to re-invert stiffness matrix  $\mathbf{K}_{\mathcal{W}}$ , where  $n$  is the total number of mesh nodes. This is similar to the Capacitance Matrix strategy presented by James and Pai in [38].

Displacement boundary conditions constrain tissue nodes to the needle geometry; whereas, force boundary conditions and thresholds impose the needle shaft force distribution estimated from physical experiments. The desired force distribution is integrated along the needle geometry, from tip to insertion/entry point, and lumped at tissue nodes that are in contact with the shaft.

## V. NON-CONFORMING NEEDLE TRAJECTORIES

In general the needle may not pass along element edges, or be coincident with mesh nodes. Three approaches for effecting nonconforming trajectories are discussed in this section.

### A. Node “Snapping”

A simple remedy is to force the tissue model to conform to the needle geometry, such that mesh nodes “snap” to the needle shaft as it passes. This amounts to setting the lateral displacement constraints along the  $^1x$  axis in order to place the closest tissue nodes onto the needle shaft, as illustrated in Fig. 6. When the needle tip begins to slip past the most distal contact node, the locations of neighboring nodes  $\mathcal{N}$  are computed so that subsequent intercepts can be identified. The displacement of each neighboring node  $j \in \mathcal{N}$  is computed as follows:

$$\begin{bmatrix} u_i^x \\ u_i^y \end{bmatrix} = \sum_{j \in \mathcal{W}} \begin{bmatrix} k_{(2i,2j)} & 0 \\ 0 & k_{(2i+1,2j+1)} \end{bmatrix} \begin{bmatrix} f_j^x \\ f_j^y \end{bmatrix} \quad (10)$$

where  $[f_j^x \ f_j^y]^T$  is the force vector at the  $j$ th node ( $j \in \mathcal{W}$ ).  $k_{(i,j)}$  is the element at row  $i$  and column  $j$  of  $(\mathbf{K}^{-1})_0$ . A pre-computed, indexed connectivity list is used to determine the set

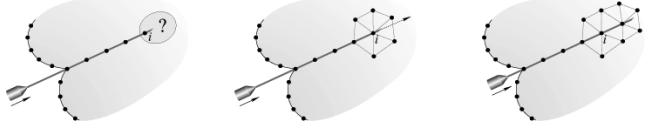


Fig. 6. New intercept nodes are identified by searching within a small neighborhood centred at the most distal needle node (see box 1 of Fig. 22).



Fig. 7. Mesh subdivision.

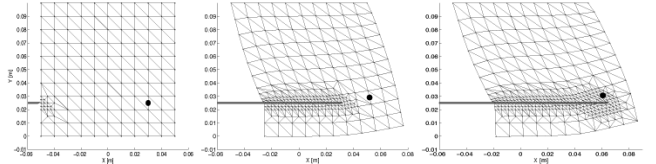


Fig. 8. Simulated needle intercept of a small target embedded within elastic tissue.

of nodes  $\mathcal{N}$  that are connected to the most distal node, as shown. When the needle tip moves outside of the elements defined by the vertices in  $\mathcal{N}$ , then the closest neighboring node is selected, and constrained to lie at the needle tip, starting in the *stuck* state. The drawback of this approach is that it can produce large local tissue deformations and force discontinuities, particularly when the tissue mesh is coarse and the tissue stiffness is high. Instead, needle and tissue geometries can be matched by subdividing or adapting the tissue mesh, as described below (this occurs in box 2 of Fig. 22).

### B. Mesh Subdivision

Mesh elements can be progressively subdivided in order to concentrate node density around the needle axis, as shown in Fig. 7. Mesh elements can either be subdivided in a uniform manner to place new mesh nodes at predetermined locations within divided elements, or they can be subdivided in order to introduce new nodes that are exactly coincident with the needle shaft.

In the simulation example shown in Fig. 8, a needle is inserted into the side of a tissue model that is rigidly fixed along one edge (the top edge as shown in the figure). Elements in the vicinity of the needle are subdivided using edge bisection; therefore, new mesh nodes are introduced closer to the needle shaft, but not necessarily coincident with it. Mesh elements can be recursively subdivided until the mesh nodes adjacent to the needle shaft are sufficiently close (i.e., on the order of the needle diameter). In the example, elements are subdivided twice and thereafter the closest nodes are simply constrained to the needle shaft. The drawback of the subdivision approach is that it can cause changes in mesh topology that require significant re-computation of the discretised material models.

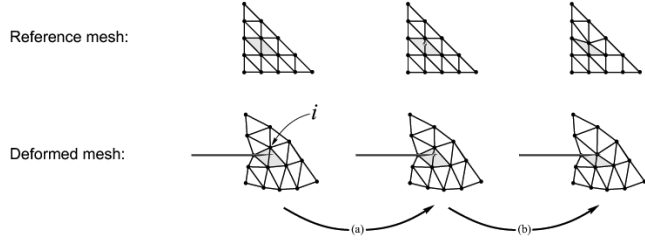


Fig. 9. (a) During simulation, as the needle tip moves from one element into another, the intersection point between the needle axis and the common edge is determined. (b) The node closest to this intersection point, node  $i$ , is projected onto the needle axis, along the direction of the common edge, by moving the nominal position of the candidate node in the nominal reference mesh such that it lies on the needle axis in the deformed mesh state.

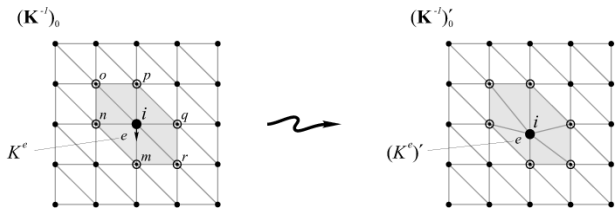


Fig. 10. The relocation of node  $i$  affects the set of connected elements  $\mathcal{E}$  (shaded).

### C. Mesh Adaptation

An alternative approach is to locally adapt existing mesh nodes so that they are coincident with the needle geometry. Instead of pulling a mesh node onto the needle by deforming the tissue model, the nominal reference mesh is adjusted so that the node is coincident with the needle. Thereafter, the node can be constrained to the needle shaft without consequence. This is illustrated in Fig. 9.

The relocation of one mesh node in the tissue model discretization affects only the elements that share it as a vertex, as shown in Fig. 10. This set of elements  $\mathcal{E}$  corresponds to a submatrix within the stiffness matrix  $\mathbf{K}$  that must be updated due to the new discretization. Each discrete element on the material domain  $\Omega$  results in a relationship of the following form:

$$\underline{\mathbf{f}}^e = K_{(6 \times 6)}^e \underline{\mathbf{u}}^e. \quad (11)$$

The element stiffness matrix  $K^e$  describes the force-displacement relationship for a single element in isolation.  $\mathbf{K}$  is the composite of element stiffness matrices over the entire body. The relocation of one node, as shown in Fig. 10, requires changes in the stiffness matrices for all elements in  $\mathcal{E}$ . For example, consider the element  $e$  with vertices  $i, m$ , and  $n$  in Fig. 10.  $K^e$  and  $(K^e)'$  are the  $(6 \times 6)$  stiffness matrices for element  $e$ , computed before and after node  $i$  is relocated, respectively, and  $\Delta K^e = (K^e)' - K^e$ . A single element update results in the following rank-6 update of  $\mathbf{K}$ :

$$\mathbf{K}' = \mathbf{K} + V \Delta K^e V^T. \quad (12)$$

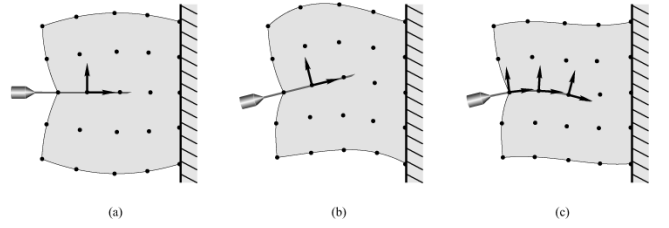


Fig. 11. Trajectory changes (b) and deflection (c) cause local changes in needle orientation.

$V$  is a  $(2N \times 6)$  selection matrix that samples  $K^e$  from  $\mathbf{K}$ , and is defined as follows:

$$[V]_{kl} = \begin{cases} 1, & \text{if } k = \mathcal{L}_l \\ 0, & \text{otherwise} \end{cases} \quad (13)$$

where  $N$  is the total number of nodes in the model discretization,  $\mathcal{L}$  is an ordered list of row indexes in  $\mathbf{K}$  that correspond to the rows of  $K^e$ , and  $\mathcal{L}_l$  is the  $l$ th entry in this list. The inverse matrix  $\mathbf{K}^{-1}$  is required for simulation, and can be computed using the *matrix inversion lemma* (Sherman-Morrison-Woodbury formula) [44] as follows:

$$(\mathbf{K} + V \Delta K^e V^T)^{-1} = \mathbf{K}^{-1} - \mathbf{K}^{-1} V \Delta K^e \times (I + V^T \mathbf{K}^{-1} V \Delta K^e)^{-1} V^T \mathbf{K}^{-1}. \quad (14)$$

Equation (14) requires the inverse of  $(I + V^T \mathbf{K}^{-1} V \Delta K^e)_{(6 \times 6)}$ , but avoids having to re-invert  $\mathbf{K}_{(2N \times 2N)}$ . For element  $e$  in the example,  $\mathcal{L} = (2i-1, 2i, 2m-1, 2m, 2n-1, 2n)$ . The remaining five elements in  $\mathcal{E}$  are updated in the same manner. Note that it is more efficient to update the six element stiffness matrices simultaneously, by means of a single rank-14 update, rather than six individual rank-6 updates. The resulting matrix  $\mathbf{K}^{-1}$  replaces  $(\mathbf{K}^{-1})_0$ . This procedure can also be implemented as a sequence of boundary condition changes (9) and matrix updates  $\Delta K^e$  made to  $(\mathbf{K}^{-1})_0$ .

### VI. LOW RANK MATERIAL COORDINATE UPDATES

The coordinate system shown in Fig. 3 is fixed to the needle; therefore, as its orientation changes it is necessary to effect local coordinate changes in  $\mathbf{K}_W^{-1}$  (this occurs in boxes 3 and 6 of Fig. 22). Needle orientation changes, curved and flexible needles cause local changes in the constraint frames, as illustrated in Fig. 11. Consider a material coordinate change at a single tissue model node  $i$ . If the boundary conditions are uniform (i.e., a force or displacement constraint along both the  ${}^1x$ - and  ${}^1y$ -axes), then  $\mathbf{K}_W^{-1}$  undergoes a transformation of coordinates as follows:

$$\begin{aligned} {}^0 \underline{\mathbf{u}}_W &= \mathbf{K}_W^{-1} {}^0 \underline{\mathbf{f}}_W \\ \Rightarrow {}^1 \underline{\mathbf{u}}_W &= A^T \mathbf{K}_W^{-1} A {}^1 \underline{\mathbf{f}}_W = (\mathbf{K}_W^{-1})' {}^1 \underline{\mathbf{f}}_W \end{aligned} \quad (15)$$

where  ${}^0 \underline{\mathbf{u}}_W$  and  ${}^0 \underline{\mathbf{f}}_W$  are displacement and force vectors in a nominal system coordinate frame, while  ${}^1 \underline{\mathbf{u}}_W$  and  ${}^1 \underline{\mathbf{f}}_W$  are the vectors after rotating the coordinate frame at the  $i$ th node by an

angle  $\theta$ . Matrix  $A$  is composed of  $(2 \times 2)$  rotation submatrices on its diagonal, and has the following form:

$$A = \begin{bmatrix} 1 & 0 & \cdots & 0 & 0 & \cdots & 0 \\ 0 & 1 & & 0 & 0 & & 0 \\ \vdots & \ddots & & & & & \vdots \\ 0 & 0 & \cos(\theta) & -\sin(\theta) & 0 & & 0 \\ 0 & 0 & \sin(\theta) & \cos(\theta) & 0 & & 0 \\ \vdots & & & & \ddots & & \vdots \\ 0 & 0 & \cdots & 0 & 0 & \cdots & 1 \end{bmatrix}. \quad (16)$$

If node  $i$  has different boundary conditions along its two coordinate axes, then such a transformation is not possible, due to the mixed force and displacement variables in  $\underline{\mathbf{x}}_{\mathcal{W}}$  and  $\underline{\mathbf{y}}_{\mathcal{W}}$ . For example, if the  $i$ th node is sliding along the needle axis, then the model equations are expressed as shown in (6), with  $\underline{\mathbf{x}}_{\mathcal{W}}$  and  $\underline{\mathbf{y}}_{\mathcal{W}}$  defined in (8). A coordinate frame rotation at the  $i$ th node is expressed as follows:

$$\begin{bmatrix} {}^0u_i^x \\ {}^0u_i^y \end{bmatrix} = \begin{bmatrix} \cos(\theta) & -\sin(\theta) \\ \sin(\theta) & \cos(\theta) \end{bmatrix} \begin{bmatrix} {}^1u_i^x \\ {}^1u_i^y \end{bmatrix}$$

$$\begin{bmatrix} {}^0f_i^x \\ {}^0f_i^y \end{bmatrix} = \begin{bmatrix} \cos(\theta) & -\sin(\theta) \\ \sin(\theta) & \cos(\theta) \end{bmatrix} \begin{bmatrix} {}^1f_i^x \\ {}^1f_i^y \end{bmatrix} \quad (17)$$

where  $[{}^0u_i^x \ {}^0u_i^y]^T$  and  $[{}^0f_i^x \ {}^0f_i^y]^T$  are the displacement and force vectors of node  $i$  before the coordinate frame change, and  $[{}^1u_i^x \ {}^1u_i^y]^T$  and  $[{}^1f_i^x \ {}^1f_i^y]^T$  are the displacement and force vectors of node  $i$  after the frame is rotated by an angle  $\theta$ . The local coordinate transformation is derived by substituting (17) into (6)

$$M^1\underline{\mathbf{x}}_{\mathcal{W}} + N^1\underline{\mathbf{y}}_{\mathcal{W}} = (\mathbf{K}_{\mathcal{W}}^{-1})' \left[ N^1\underline{\mathbf{x}}_{\mathcal{W}} + M^1\underline{\mathbf{y}}_{\mathcal{W}} \right]$$

$$\Rightarrow {}^1\underline{\mathbf{x}}_{\mathcal{W}} = \left[ M - (\mathbf{K}_{\mathcal{W}}^{-1})' N \right]^{-1} [\mathbf{K}_{\mathcal{W}}^{-1} M - N] {}^1\underline{\mathbf{y}}_{\mathcal{W}} \quad (18)$$

where  $M$  and  $N$  are sparse transformation matrices that have the following form:

$$M = \begin{bmatrix} 1 & 0 & \cdots & 0 & 0 & \cdots & 0 \\ 0 & 1 & & 0 & 0 & & 0 \\ \vdots & \ddots & & & & & \vdots \\ 0 & 0 & \cos(\theta) & 0 & 0 & & 0 \\ 0 & 0 & 0 & \cos(\theta) & 0 & & 0 \\ \vdots & & & & \ddots & & \vdots \\ 0 & 0 & \cdots & 0 & 0 & \cdots & 1 \end{bmatrix}$$

$$N = \begin{bmatrix} 0 & 0 & \cdots & 0 & 0 & \cdots & 0 \\ 0 & 0 & & 0 & 0 & & 0 \\ \vdots & \ddots & & & & & \vdots \\ 0 & 0 & 0 & -\sin(\theta) & 0 & & 0 \\ 0 & 0 & \sin(\theta) & 0 & 0 & & 0 \\ \vdots & & & & \ddots & & \vdots \\ 0 & 0 & \cdots & 0 & 0 & \cdots & 0 \end{bmatrix}. \quad (19)$$

In (18), the local coordinate transformation for a single node that is in the *slip* state requires that  $(M - \mathbf{K}_{\mathcal{W}}^{-1}N)$  be inverted. This matrix inverse is shown to be sparsely populated, with an analytical inverse given by

$$(M - \mathbf{K}_{\mathcal{W}}^{-1}N)^{-1} = \begin{bmatrix} 1 & 0 & \cdots & a_{(1,2i)} & a_{(1,2i+1)} & \cdots & 0 \\ 0 & 1 & & a_{(2,2i)} & a_{(2,2i+1)} & & 0 \\ \vdots & \ddots & & & & & \vdots \\ 0 & 0 & a_{(2i,2i)} & a_{(2i,2i+1)} & 0 & & 0 \\ 0 & 0 & a_{(2i+1,2i)} & a_{(2i+1,2i+1)} & 0 & & 0 \\ \vdots & & & & \ddots & & \vdots \\ 0 & 0 & \cdots & a_{(2s,2i)} & a_{(2s,2i+1)} & \cdots & 1 \end{bmatrix} \quad (20)$$

where

$$a_{(1,2i)} = -\frac{\sin \theta [k_{(1,2i+1)} (\cos \theta + k_{(2i+1,2i)} \sin \theta)]}{\sum} + \frac{\sin \theta [k_{(1,2i)} k_{(2i+1,2i+1)} \sin \theta]}{\sum}$$

$$a_{(1,2i+1)} = \frac{\sin \theta [k_{(1,2i)} (\cos \theta - k_{(2i,2i+1)} \sin \theta)]}{\sum} + \frac{\sin \theta [k_{(1,2i+1)} k_{(2i,2i)} \sin \theta]}{\sum}$$

$$a_{(2i,2i)} = -\frac{\cos \theta + k_{(2i+1,2i)} \sin \theta}{\sum}$$

$$a_{(2i,2i+1)} = \frac{k_{(2i,2i)} \sin \theta}{\sum}$$

$$a_{(2i+1,2i)} = -\frac{k_{(2i+1,2i+1)} \sin \theta}{\sum}$$

$$a_{(2i+1,2i+1)} = \frac{-\cos \theta + k_{(2i,2i+1)} \sin \theta}{\sum}$$

$$\sum = -\cos^2 \theta + \cos \theta \sin \theta (k_{(2i,2i+1)} - k_{(2i+1,2i)}) + \sin^2 \theta (k_{(2i,2i+1)} k_{(2i+1,2i)} - k_{(2i,2i)} k_{(2i+1,2i+1)}) \quad (21)$$

and  $k_{(m,n)}$  is the element at the  $m$ th row and  $n$ th column of  $\mathbf{K}_{\mathcal{W}}^{-1}$ . If the needle is rigid and straight, then the rotation angle  $\theta$  is constant for all tissue nodes in contact with the needle shaft. If the needle is curved or flexible, then  $\theta$  varies according to the shaft geometry.

Local material coordinate frames at all contact nodes in  $\mathcal{W}$  are updated incrementally from one simulation step to the next, according to the change in needle orientation angle  $\Delta\theta$ . If the needle is curved or flexible, then the local coordinate system transformations will vary along the length of the needle shaft.

## VII. NEEDLE FLEXIBILITY

Needles used for fine needle aspiration biopsy, certain types of nerve blocks, and brachytherapy are long, thin and flexible. In many cases, needle deflection has a significant impact on placement accuracy. An elastic model describes the bending of stainless steel needles in a manner similar to that used to describe the tissue phantom. In two dimensions, the needle is modeled

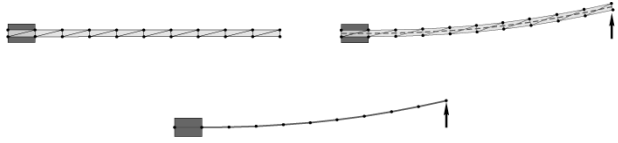


Fig. 12. The needle is represented by a linear elastic beam.

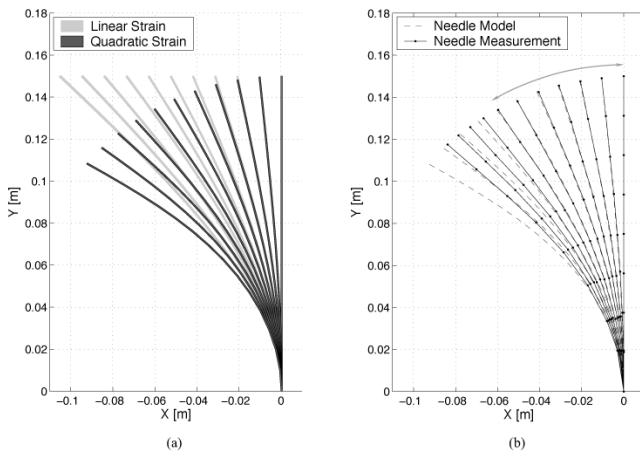


Fig. 13. Needle elasticity model with: (a) a comparison of linear and quadratic strain models, and (b) physical validation of the quadratic strain model against measured deflections of a 15 cm, 20 gauge biopsy needle.

as a thin elastic beam, as illustrated in Fig. 12. The constitutive equations are discretised using the Finite Element Method. Since the needle is long and slender, even modest deflections result in large global deformations and high strains. The small strain assumption that is made in order to use the linear Cauchy strain tensor is not valid for such global deformations; therefore, the Green-Lagrange strain formulation is used. This is also referred to as quadratic strain [45], [46]. The practical relevance of these two formulations is illustrated in Fig. 13(a), which shows simulated needle deformations due to a range of tip forces applied along the X-axis, using both linear (Cauchy) and quadratic (Green-Lagrange) strain (the needle model is fixed at its base). The linear strain model does not preserve element volume—and hence needle length—for large strains, and is not rotation independent; therefore, it performs poorly.

Physical measurements of planar needle deflections were obtained experimentally, and used to fit a 2-D needle model derived using linear elasticity and quadratic strain. A 20 gauge, 15 cm *Chiba* biopsy needle was mounted horizontally, and fixed at its base by means of a clamp. A linear motion stage, instrumented with a force sensor (ATI Nano-17), was used to apply constant lateral forces—ranging from 0.05 N to 0.5 N—at the needle tip, while planar displacement/deflection was measured at several points along the needle shaft. The needle model is represented by a mesh of triangular elements with  $16 \times 4$  nodes, and a linear constitutive model with Young's modulus and Poisson ratio determined from a best fit to the empirical data, as shown in Fig. 13(b). Their values (980 MPa and 0.3, respectively) compensate for differences between needle and model mesh geometry (due to meshing constraints), and are therefore do not match expected values for steel. Measured and computed needle displacements agree within approximately

2% over a large range of needle deflections. For tip deflections greater than 60 mm, the needle appears to begin stiffening and the model becomes inaccurate.

The set of nonlinear model equations that describe the relationship between applied needle node forces and node displacements are expressed as

$$\begin{aligned} \underline{\mathbf{f}}_n &= \mathbf{K}_n(\underline{\mathbf{u}}_n)\underline{\mathbf{u}}_n \\ \Rightarrow \underline{\mathbf{f}}_n &= \left( (\mathbf{K}_n)_0 + \frac{1}{2} \int_{\Omega} B^T CAG d\Omega \right) \underline{\mathbf{u}}_n \\ \Rightarrow \underline{\mathbf{f}}_n &= (\mathbf{K}_n)_0 \underline{\mathbf{u}}_n + (\underline{\mathbf{f}}_n)_q \end{aligned} \quad (22)$$

where the “stiffness matrix”  $\mathbf{K}_n(\underline{\mathbf{u}}_n)$  is a nonlinear function of displacement.  $(\mathbf{K}_n)_0$  is the matrix of linear stiffness components, while the integral introduces higher order terms due to quadratic strain, as detailed in [37]. Needle node forces  $\underline{\mathbf{f}}_n$  are expressed as the sum of forces due to linear strain and forces due to quadratic strain,  $(\underline{\mathbf{f}}_n)_q$ . If force boundary conditions are applied to the needle model, then (22) can be inverted by means of the following iterative numerical method

$$(\underline{\mathbf{u}}_n)_{i+1} = (\mathbf{K}_n)_0^{-1} [\underline{\mathbf{f}}_n - (\underline{\mathbf{f}}_n)_q((\underline{\mathbf{u}}_n)_i)] \quad (23)$$

where  $(\underline{\mathbf{u}}_n)_0 = \mathbf{0}$ , and  $\underline{\mathbf{f}}_n$  is a vector of external force constraints applied at needle nodes (needle deflection is computed in box 8 of Fig. 22). For the model shown in Fig. 13,  $(\underline{\mathbf{u}}_n)_i$  converges to within 0.1% of  $\underline{\mathbf{u}}_n$  by the 10th iteration of (23), when a tip force of  $-0.3N$  is applied along the X-axis.

## VIII. SOLVING THE COUPLED NEEDLE AND TISSUE MODELS

At each simulation time step, the vector of unknown forces and displacements at *working nodes* are calculated as follows:

$$\underline{\mathbf{x}}'_{\mathcal{W}} = (\mathbf{K}_{\mathcal{W}}^{-1})' \underline{\mathbf{y}}'_{\mathcal{W}} \quad (24)$$

where  $(\mathbf{K}_{\mathcal{W}}^{-1})'$  is the updated system matrix after all boundary condition changes and local coordinate frame changes have been computed at each contact tissue node, using fast low-rank update methods. The specified constraint vector  $\underline{\mathbf{y}}'_{\mathcal{W}}$  and the vector of free variables  $\underline{\mathbf{x}}'_{\mathcal{W}}$  contain node displacement and force coordinates for each observed node, expressed in their local material coordinate frames. The vector of unknown node forces and displacements,  $\underline{\mathbf{x}}'_{\mathcal{W}}$ , is computed in (24), and then reconstituted into displacement and force vectors expressed in a reference coordinate frame, based on the known boundary conditions and coordinate frames at each node (the tissue model is solved in box 7 of Fig. 22).

The needle is represented by the midline of the needle model shown in Fig. 12. Forces at contact/working nodes on the tissue model are projected onto the needle model in order to compute the deflection of needle nodes,  $\underline{\mathbf{u}}_n$  according to (23). The resulting configuration of the needle line segment in turn applies new displacement constraints on the tissue contact nodes. With appropriate damping, the coupled system reaches equilibrium within several simulation steps. In the examples given here, a velocity gain of 0.033 is applied at each needle model node (i.e.,  $(\underline{\mathbf{x}}_n)_k = (\underline{\mathbf{x}}_n)_{k-1} + 0.033\Delta\underline{\mathbf{x}}_n$ , where  $(\underline{\mathbf{x}}_n)_k$  is the compound vector of needle node coordinates at the  $k$ th simulation step),

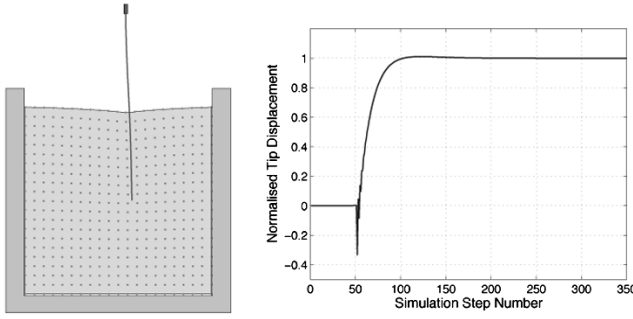


Fig. 14. A step test illustrates the convergence of coupled needle and tissue models.

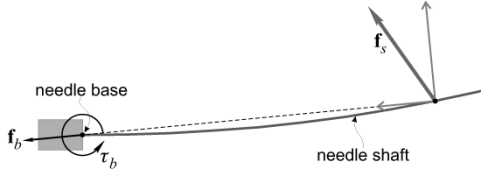


Fig. 15. Contact forces that occur along the needle shaft are referred to the needle base and integrated to obtain the resultant driving forces and moments.

with a sample time of 2 ms. Fig. 14 illustrates the system convergence after a step test; after a straight-line insertion, the needle base is stepped 3 mm to the left. A normalized plot of lateral displacement at the needle tip indicates a damped response as the coupled system reaches the coupled system reaches within 1% of equilibrium after approximately 50 simulation steps (0.1 s). This is sufficiently fast for the transients to go unnoticed by the user.

Contact forces that occur along the needle shaft are integrated to determine the resultant driving force at the needle base (box 9 of Fig. 22). The force vector computed at each contact node is decomposed as shown in Fig. 15, and referred to a coordinate frame located at the base. Base forces and torques resulting from each contact node are summed to produce the resultant driving force  $\mathbf{f}_b$  and torque  $\tau_b$ . Examples of base driving forces and torques for a simulated needle insertion trajectory are graphed in Fig. 16.

For straight, rigid needle models, the forces are summed as follows:

$${}^0 \begin{bmatrix} \mathbf{f}_b \\ \tau_b \end{bmatrix} = \sum_{i \in \mathcal{W}} \begin{bmatrix} \cos(\theta_i) & -\sin(\theta_i) \\ \sin(\theta_i) & \cos(\theta_i) \\ |\tilde{\omega}_i - \tilde{\omega}_o| & 0 \end{bmatrix} {}^1 \mathbf{f}_i \quad (25)$$

where  $\tilde{\omega}_i$  is the location of the  $i$ th node and  $\tilde{\omega}_o$  is the location of the needle base, so that  $|\tilde{\omega}_i - \tilde{\omega}_o|$  is the axial distance between the node and the needle base. The total wrench  ${}^0 [\mathbf{f}_b \ \tau_b]^T$  is expressed in terms of a fixed environment coordinate frame, while the node force vector  ${}^1 \mathbf{f}_i$  lies in the local coordinate frame at node  $i$ , which is rotated by an angle of  $\theta_i$  with respect to the fixed reference frame.

The set  $\mathcal{V}$  of tissue model displacements at nodes that are not in  $\mathcal{W}$ , but that are required for visualization, are computed as follows:

$$\underline{\mathbf{u}}_{\mathcal{V}} = [(\mathbf{K}^{-1})_0]_{\mathcal{V}, \mathcal{W}} \underline{\mathbf{f}}_{\mathcal{W}} \quad (26)$$

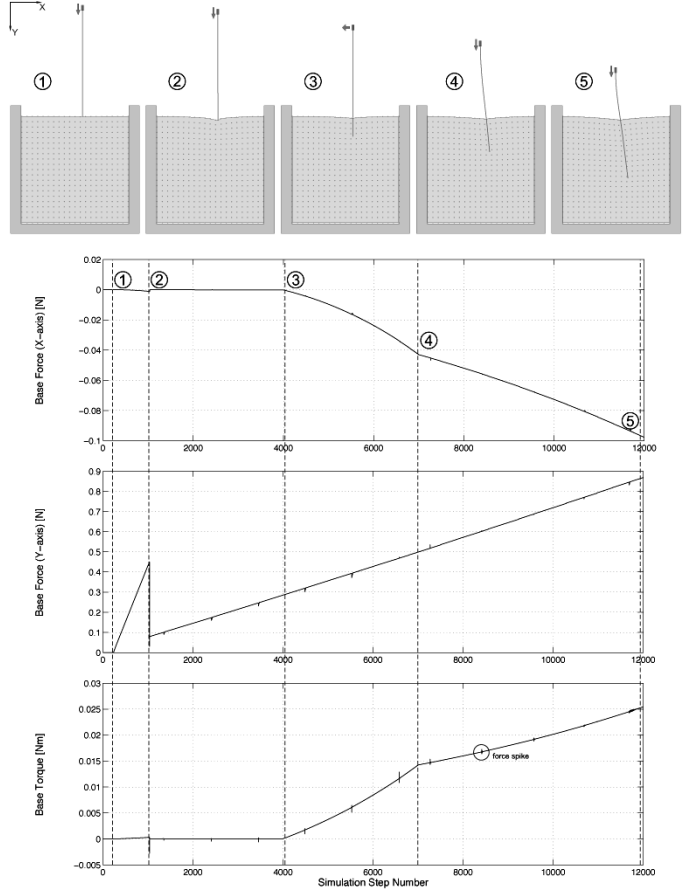


Fig. 16. An example of the base forces and torques required to drive the needle along a simulated insertion trajectory. The trajectory proceeds as follows: (1) the needle tip makes contact with the tissue model, (2) the needle punctures the model surface and insertion continues along the  $y$ -axis, (3) insertion continues along the  $y$ -axis, with lateral base motion along the  $-x$ -axis, (4) insertion continues along the  $y$  axis only, and (5) end of insertion. Small force spikes occur while the system converges after new working nodes are added.

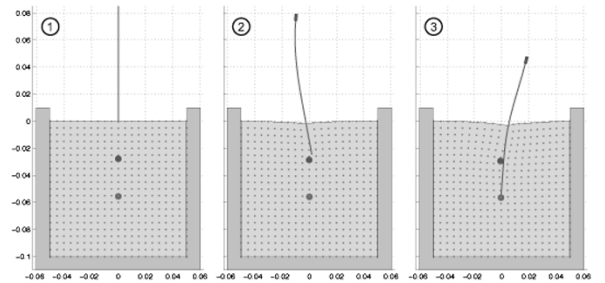


Fig. 17. Simulation of a nonlinear steered needle trajectory. The base of the needle is manipulated in order to simulate steering around an obstacle.

where  $\underline{\mathbf{u}}_{\mathcal{V}}$  is a vector of displacement variables that are required and  $\underline{\mathbf{f}}_{\mathcal{W}}$  is the vector of forces at working nodes (known from (24) and the applied boundary constraints).  $[(\mathbf{K}^{-1})_0]_{(\mathcal{V}, \mathcal{W})}$  is the matrix that contains rows and columns corresponding to the variables in  $\mathcal{V}$  and the nodes in  $\mathcal{W}$ , respectively.

Further examples of simulated needle trajectories are provided in Figs. 17 and 18. Fig. 17 illustrates a complex nonlinear needle insertion required to steer the needle around an obstacle [47], [48], while Fig. 18 shows an oblique insertion trajectory in an inhomogeneous tissue model.

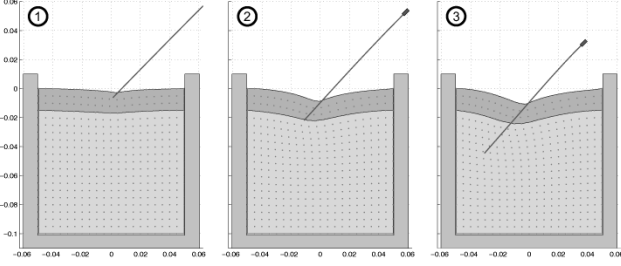


Fig. 18. An oblique needle trajectory into a nonhomogeneous tissue model (stiff surface layer).

TABLE I  
MODEL AND ALGORITHM SPECIFICATIONS FOR HAPTIC SIMULATION

Material Type	linear elastic, isotropic, $100^2 \times 11\text{mm}$
Young's Modulus	inhomogeneous
Poisson Ratio	0.48
Number of Nodes	361 ( $19 \times 19$ )
Element Type	3-node triangle, plane stress
Strain	Cauchy, linear strain approximation
Needle Model	rigid
Mesh Subdivision	none
Mesh Adaptation	none (nodes "snap" to needle)
Model Sample Rate	512Hz

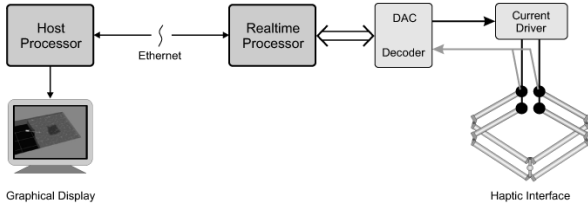


Fig. 19. Haptic simulation hardware system.

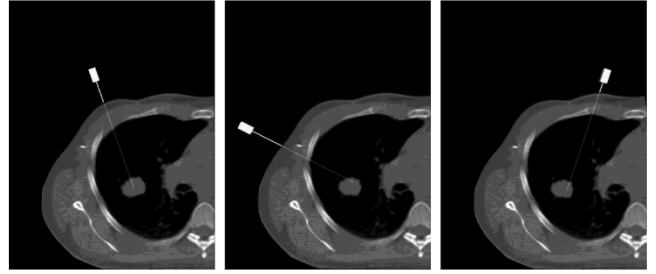


Fig. 21. Interactive virtual lung nodule biopsy.

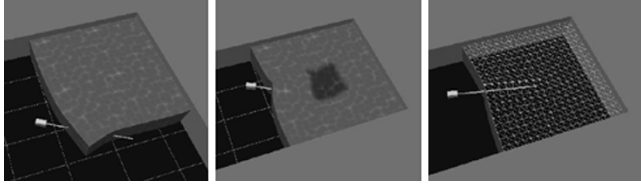


Fig. 20. Interactive virtual needle insertion in a planar environment.

## IX. HAPTIC NEEDLE INSERTION

A real-time implementation of the needle insertion simulation algorithm allows users to experience both visual and kinesthetic feedback while executing a virtual planar needle insertion. The haptic simulation algorithm is based on the techniques described in Sections II–VIII, with the exception of the needle model, which is currently assumed to be rigid in order to achieve model computations at haptic rates. In addition, a “node snapping” technique (see Section V-A) is used instead of mesh adaptation. The system comprises a host processor with a graphical display, a real-time processor, and a haptic interface with its associated input–output (I/O) interfaces and power amplifiers, as illustrated in Fig. 19. Both the host and real-time processors are standard 1-GHz Pentium PCs. The haptic interface is similar to the planar pantograph mechanism that is used to manipulate the needles during insertion experiments, and is controlled by a real-time processor, as described in [37], [43]. A Quanser MultiQ-PCI interface facilitates I/O between the haptic interface and the real-time processor. The visual environment is rendered by the host processor, which receives the needle and tissue model states from the real-time processor via an Ethernet connection.

The low-rank numerical operations require  $O(s^2)$  computations per sample period in order to compute the needle insertion models, where  $s$  is the number of contact or *working nodes* in  $\mathcal{W}$ . In contrast, a simulation involving all nodes in the discretised tissue volume, with full matrix inversions, would require

$O(n^3)$  computations, where  $n$  is the total number of mesh nodes ( $n \gg s$ ). Displacements at all tissue model nodes are computed in order to graphically render the complete deformation state of the model; therefore, a further  $O(ns)$  computations are required.

Fig. 20 presents a series of display snapshots taken during interactive virtual needle insertion in a planar environment, with a 361-node tissue model computed at 512 Hz, and a rigid needle model. The model and algorithm specifications are summarized in Table I. Both the model simulation and haptic interface control algorithms are computed by the real-time processor under the VxWorks operating system, without any particular effort to optimize code. Contact forces and torques are fed back to the operator via the haptic interface, as facilitated by a four-channel control architecture that is described in [49] and [37].

An example of a simulated lung nodule biopsy is shown in Fig. 21. The tissue geometry was taken from a segmented computed tomography (CT) image, while tissue parameters were chosen in an ad hoc manner, guided by values published in the literature.

## X. DISCUSSION

The simulation algorithm is physically based, but under specific conditions only. A user may command arbitrary needle velocities and may choose to insert and retract the needle. The slip force thresholds are set according to the shaft force distribution derived for insertions at a single velocity [43]. Therefore, simulated needle forces closely match measured values for insertions at this velocity. The force-velocity relationships given in [36], can be used to adjust the force distribution according to insertion velocity. Velocity dependence and the slip-stick contact model introduce dynamic behavior into the simulation, despite the quasi-static tissue model. An algorithm flow chart for the simulation algorithm is given in Fig. 22.

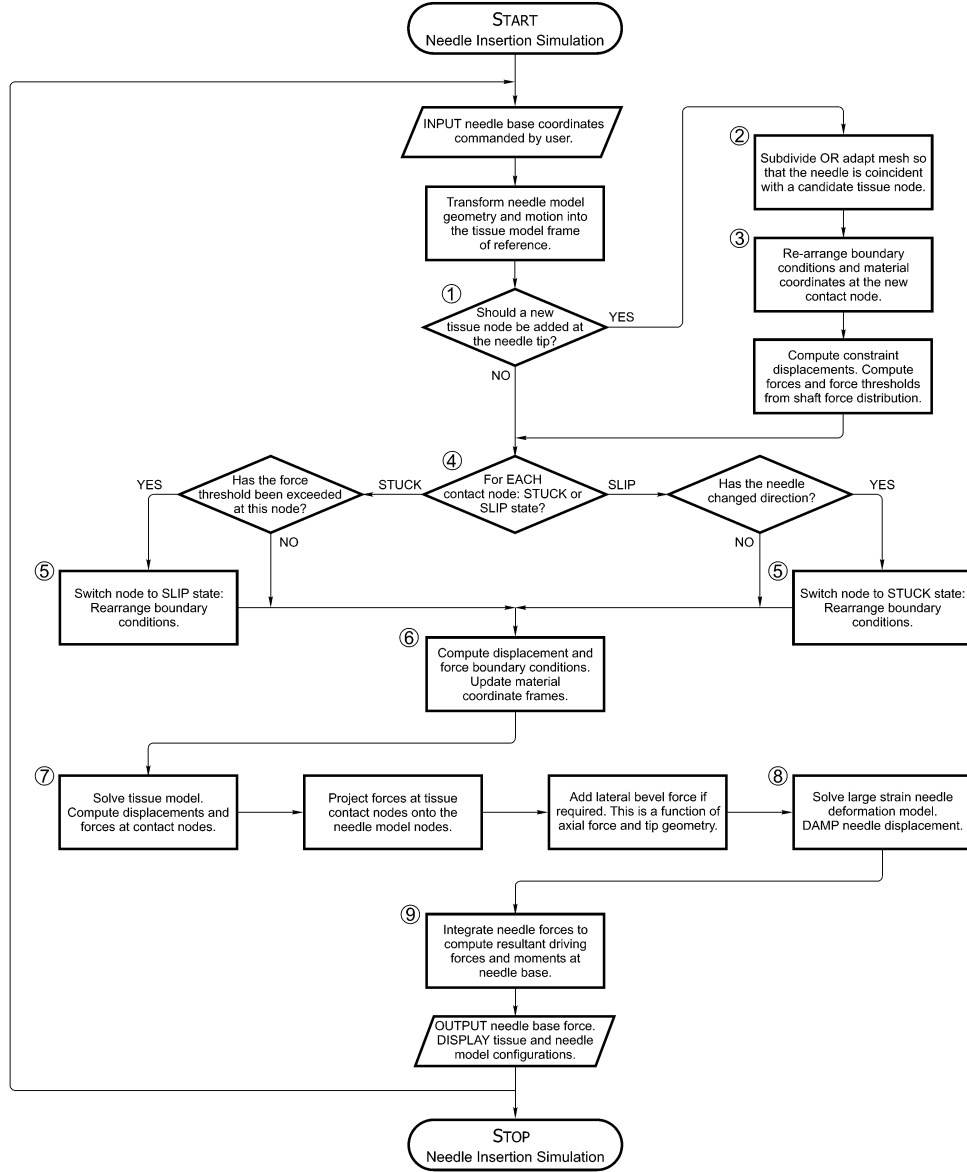


Fig. 22. An overview of the needle insertion simulation algorithm. References for numbered boxes are indexed in Table II.

TABLE II  
FLOWCHART INDEX

Box Number	Reference
1	Section V, Figure 6
2	Section V-B, V-C
3	Equation (9), Equation (15), Equation (18)
4	Section IV, Figure 4
5	Equation (9)
6	Equation (15), Equation (18)
7	Equation (24)
8	Equation (23)
9	Section VIII

The discretised linear elastostatic model has worked well for haptic needle insertion. Local phantom stresses due to the observed needle force distribution are fairly low, so that axial strains are low. There is little lateral motion and rotation during typical needle trajectories; however, users are not constrained during haptic simulation and may generate large strains.

The needle insertion simulation algorithm can fail under certain circumstances, as outlined below.

- The simulation algorithm will fail when tissue model elements are forced to collapse/invert due to excessive lateral needle motion and large strains. In the haptic environment, this situation is prevented by limiting the maximum needle force that can be applied by the user.
- High needle velocity can cause the collision detection between needle and tissue mesh elements to fail due to excessive displacement in a single time step. In practice, this occurs at insertion velocities higher than the upper limit observed in clinical applications (approx. 20 mm/s).
- The haptic simulation fails when the real-time system cannot maintain its 512 Hz sample rate. Complexity of computation increases with the number of tissue nodes in contact with the needle (i.e., as the dimension of  $K_W$  increases), thereby limiting the depth of needle insertion.
- Boundaries between very soft and very stiff elements can cause instability, due to large force discontinuities.

- The simulation will fail if the coupled system is inadequately damped, or if model parameters are physically infeasible. Stability is particularly sensitive to the elasticity of needle versus tissue models, and it is easy to choose model parameters that are physically infeasible (e.g., a needle model with much lower stiffness than tissue, where a physical needle would buckle.)

The 2-D models and planar motion are unable to simulate the deformations of true 3-D anatomically based systems, or to present anatomical geometries for trajectory selection. However, in its present form, the simulator exhibits relevant perceptual cues as the needle penetrates tissue boundaries in inhomogeneous models, albeit in two dimensions. Once a needle trajectory has been chosen through the tissue, most clinical needle insertions today are still linear (i.e., the needle is not intentionally steered); therefore, the choice of two dimensions as a first pass at the problem is not too much of an oversimplification, in terms of establishing insertion mechanics and hence the ability to establish stereognosis.

Feedback from the medical community has been very positive, despite rather simple model geometries. Physicians specialising in a variety of areas, including anaesthesia, oncology (biopsy and brachytherapy), and surgery have evaluated the simulator; however, a controlled user survey has not yet been undertaken to quantify their feedback.

## XI. SUMMARY AND CONCLUSIONS

In this paper, fast numerical techniques have been developed in order to solve coupled linear needle and tissue models for insertion simulations at interactive rates. This has led to a number of analytical advances.

- It is shown that boundary conditions need only be explicitly considered at the small subset of tissue model nodes that are in contact with the needle. The number of system variables is reduced by means of a matrix condensation approach. Unlike previous applications of this technique, the set of variables that are explicitly considered in the condensed system evolves as the needle penetrates the tissue volume.
- Boundary condition changes are applied using low rank system updates, according to a slip-stick contact model. The boundary conditions are more complex than those seen previously for point and surface interactions, due to the volumetric interaction and the continuously evolving condensed system representation. In addition, varying constraint directions—due to needle orientation changes, curved and flexible needles—require local material coordinate changes. An analytical inverse has been derived to efficiently update material coordinate at contact nodes.
- Fast local mesh adaptations using low-rank matrix updates were developed in order to match needle and tissue mesh geometries, while avoiding computationally expensive matrix re-inversions.
- A large-strain needle model is coupled to the tissue model by matching boundary conditions, and the coupled system is solved iteratively. Needle deflections in soft tissues have been shown to have a significant impact on needle tip

placement in practice, and are simulated here for the first time.

- A compelling haptic environment, implemented based on the interactive needle insertion simulation algorithm, has been developed and demonstrated. This is the first such system to include physically based needle forces and torques, soft tissue deformation and real-time interactivity.

## XII. FUTURE WORK

The models and simulation algorithms will be generalized to 3-D, as outlined below.

- Tissue models will be discretised using volumetric elements, such as tetrahedra and hexahedra (commercial and open-source 3-D meshing algorithms are available for this). The finite element approach can be applied to volumetric elements in 3-D, resulting in a stiffness matrix and (4), as in the 2-D case.
- Matrix condensation, low-rank boundary condition updates, mesh adaptation, and low-rank material coordinate updates will be computed as before, with minor modification due to the additional dimension. Further optimization may be required to ameliorate the effects of this increased computational burden.
- An efficient 3-D beam representation of the needle is required. If the needle is represented by a set of nodes lying along the shaft axis, then tissue-needle contact boundary conditions will be computed as before. The calculation of needle-tissue intercept will be modified to take into account the new element geometry.
- Needle and tissue models will still be coupled along coincident needle and tissue nodes; however, the iterative coupling algorithm may require further development in order to ensure convergence and stability with the additional degrees of freedom.

For some practical problems involving detailed 3-D models, the size of the data-sets may exceed available memory resources, requiring hierarchical representations, data caching and predictive caching. Interactive simulations of complex tissue models in three dimensions will benefit from the multiresolution and mesh adaptation techniques described in [50] and [51].

Needle insertion simulations for medical training will be based on anatomical models and clinical procedures. While high-resolution imaging techniques, such as magnetic resonance imaging and CT, provide tractable geometric structure for anatomic models, they do not provide biomechanical parameters, boundary conditions etc. *In vivo* biomechanics studies and elastography research are ongoing, but promise to contribute such clinical data in the near future. In the meantime, model geometries can be built based on medical image data, with tissue parameters approximated from rheological data available in the literature. The effectiveness of these models, and the extent of realism required, are yet to be determined. Prototype systems should be developed with help from the medical community in order to investigate these human factors. The

contact model, working in conjunction with the force-velocity relationship measured in experiments, should also be evaluated in this context.

Many of the methods presented in this paper are independent of a specific tissue model, and may be generalizable to other—more realistic—models. The interactive simulation techniques rely on the assumption of linearity in order to achieve satisfactory real-time performance; therefore, future work will be required to extend this to nonlinear systems.

## REFERENCES

- [1] F. S. Azar, D. N. Metaxas, and M. D. Schnall, "A finite element model of the breast for predicting mechanical deformations during biopsy procedures," in *Proc. IEEE Workshop Mathematical Methods in Biomedical Image Analysis*, 2000, pp. 38–45.
- [2] J. J. Bauer, J. Zeng, I. A. Sesterhenn, J. W. Moul, and S. K. Mun, "Comparison of prostate biopsy protocols using 3-D computer simulation," in *Proc. Pacific Medical Technology Symp.*, Aug. 1998, pp. 109–114.
- [3] S. Nath, Z. Chen, N. Yue, S. Trumppore, and R. Peschel, "Dosimetric effects of needle divergence in prostate seed implant using  $^{125}\text{I}$  and  $^{103}\text{Pd}$  radioactive seeds," *Med. Phys.*, pp. 1058–1066, 2000.
- [4] J. De Andres, M. A. Reina, and A. Lopez-Garcia, "Risks of regional anaesthesia: Role of equipment—Needle design, catheters," presented at Prpc. 17th Annu. Eur. Soc. Regional Anaesthesia Congr. [Online]. Available: <http://www.esraeurope.org/andres14.htm>
- [5] P. Gorman, T. Krummel, R. Webster, M. Smith, and D. Hutchens, "A prototype haptic lumbar puncture simulator," in *Proc. Medicine Meets Virtual Reality*, 2000, pp. 106–109.
- [6] S. Datta, "Complications of regional analgesia and anaesthesia," presented at Proc. 17th Annu. Eur. Soc. Regional Anaesthesia Congr. [Online]. Available: <http://www.esraeurope.org/datta1.htm>
- [7] B. Finucane, "Complications of brachial plexus anaesthesia," presented at Proc. 17th Annu. Eur. Soc. Regional Anaesthesia Congr. [Online]. Available: <http://www.esraeurope.org/finucan1.htm>
- [8] D. L. Brown, "What do we need to advance regional anaesthesia?," presented at Proc. 17th Annu. Eur. Soc. Regional Anaesthesia Congr. [Online]. Available: <http://www.esraeurope.org/brown12.htm>
- [9] L. T. Kohn, J. M. Corrigan, and M. S. Donaldson, Eds., *To Err Is Human: Building a Safer Health System*. Washington, DC: National Academies Press, 2000.
- [10] A. Zorcolo, E. Gobbetti, P. Pili, and M. Tuveri, "Catheter insertion simulation with combined visual and haptic feedback," in *Proc. 1st PHANTOM Users Research Symp. (PURS'99)*, May 1999.
- [11] E. Gobbetti, M. Tuveri, G. Zanetti, and A. Zorcolo, "Catheter insertion simulation with co-registered direct volume rendering and haptic feedback," in *Proc. Medicine Meets Virtual Reality 2000*, Jan. 2000, pp. 96–98.
- [12] CathSim Vascular Access Simulator [Online]. Available: <http://www.immersion.com/products/medical/vascular.shtml>
- [13] M. Bro-Nielsen, J. L. Tasto, R. Cunningham, and G. L. Merrill, "PreOp™ endoscopic simulator—A PC-based immersive training system for bronchoscopy," presented at the Medicine Meets Virtual Reality 7 (MMVR-7), San Francisco, CA, 1999.
- [14] P. N. Brett, T. J. Parker, A. J. Harrison, T. A. Thomas, and A. Carr, "Simulation of resistance forces acting on surgical needles," in *J. Eng. Med.*, London, U.K.: Inst. Mech. Eng., 1997, pt. H, vol. 211, pp. 335–347.
- [15] T. Dang, T. M. Annaswamy, and M. A. Srinivasan, "Development and evaluation of an epidural injection simulator with force feedback for medical training," in *Proc. Medicine Meets Virtual Reality*, 2001, pp. 97–102.
- [16] L. Hiemenz, D. J. McDonald, D. Stredney, and D. Sessanna, "A physiologically valid simulator for training residents to perform an epidural block," in *Proc. 15th Southern Biomedical Engineering Conf.*, Mar. 1996, pp. 170–173.
- [17] L. Hiemenz, A. Litsky, and P. Schmalbrock, "Puncture mechanics for the insertion of an epidural needle," presented at Proc. 21st Annual Meeting of the American Society of Biomechanics. [Online]. Available: <http://asb-biomech.org/onlineabs/abstracts97/34/index.html>
- [18] L. Hiemenz, D. Stredney, and P. Schmalbrock, "Development of the force-feedback model for an epidural needle insertion simulator," in *Proc. Medicine Meets Virtual Reality*, 1998, pp. 272–277.
- [19] R. S. Haluck, W. B. Murray, R. Webster, N. Mohler, and M. Melkonian, "A haptic lumbar puncture simulator," presented at the Medicine Meets Virtual Reality, Newport Beach, CA, Jan. 2000.
- [20] S. K. Singh, M. Bostrom, D. O. Popa, and C. W. Wiley, "Design of an interactive lumbar puncture simulator with tactile feedback," in *Proc. IEEE Int. Conf. Robotics and Automation*, vol. 2, 1994, pp. 1734–1739.
- [21] D. O. Popa and S. K. Singh, "Creating realistic force sensations in a virtual environment: Experimental system, fundamental issues and results," in *Proc. IEEE Int. Conf. Robotics and Automation*, May 1998, pp. 59–63.
- [22] D. Kwon, J. Kyung, S. M. Kwon, J. B. Ra, H. W. Park, H. S. Kang, J. Zeng, and K. R. Cleary, "Realistic force reflection in a spine biopsy simulator," in *Proc. IEEE Int. Conf. Robotics and Automation*, 2001, pp. 1358–1363.
- [23] K. B. Shimoga and P. K. Khosla, "Visual and force feedback to aid neurosurgical probe insertion," in *16th Int. Conf. IEEE Engineering in Medicine and Biology Society*, vol. 2, 1994, pp. 1051–1052.
- [24] S. Miller, C. Jeffrey, J. Bews, and W. Kinsner, "Advances in the virtual reality interstitial brachytherapy system," in *Proc. Canadian Conf. Electrical and Computer Engineering*, May 1999, pp. 349–354.
- [25] J. Zeng, C. Kaplan, J. Bauer, J. Xuan, I. A. Sesterhenn, J. H. Lynch, M. T. Freedman, and S. K. Mun, "Optimizing prostate needle biopsy through 3-D simulation," *Proc. SPIE (Med. Imag.)*, vol. 3335, pp. 488–497, Feb. 1998.
- [26] J. Moline, "Virtual Environments for Health Care," A White Paper for the Advanced Technology Program (ATP) National Institute of Standards and Technology, Tech. Rep., Oct. 1995.
- [27] D. Sorid and S. K. Moore, "The virtual surgeon," *IEEE Spectrum Mag.*, pp. 26–31, Jul. 2000.
- [28] M. Teschner, S. Girod, and B. Girod, "Optimization approaches for soft-tissue prediction in craniofacial surgery simulation," in *Conf. Medical Image Computing and Computer-Assisted Intervention*, 1999, pp. 1183–1190.
- [29] L. M. Auer, A. Radetzky, C. Wimmer, G. Kleinszig, F. Schroeder, D. P. Auer, H. Delingette, B. Davies, and D. P. Pretschner, "Visualization for planning and simulation of minimally invasive neurosurgical procedures," in *Proc. Medical Image Computing and Computer-Assisted Intervention*, 1999, pp. 1199–1209.
- [30] A. Zivanovic and B. L. Davies, "A robotic system for blood sampling," *IEEE Trans. Inf. Technol. Biomed.*, vol. 4, no. 1, pp. 8–14, Mar. 2000.
- [31] K. Khodabandehloo, P. N. Brett, and R. O. Buckingham, "Special-purpose actuators and architectures for surgery robots," in *Computer-Integrated Surgery: Technology and Clinical Applications*. Cambridge, MA: The MIT Press, 1996.
- [32] H. Saito and T. Togawa, "Detection of puncturing vessel wall for automatic blood sampling," in *Proc. 1st Joint BMES/EMBS Conf. Serving Humanity, Advancing Technology*, Oct. 1999, p. 866.
- [33] C. Simone and A. Okamura, "Modeling of needle insertion for robot-assisted percutaneous therapy," in *Proc. IEEE Int. Conf. Robotics and Automation*, May 2002, pp. 2085–2091.
- [34] H. Kataoka, T. Washio, K. Chinzei, K. Mizuhara, C. Simone, and A. M. Okamura, "Measurement of the tip and friction force acting on a needle during penetration," in *Proc. Medical Image Computing and Computer Aided Intervention*, 2002, pp. 216–223.
- [35] R. Alterovitz, J. Pouliot, R. Taschereau, I. J. Hsu, and K. Goldberg, "Needle insertion and radioactive seed implantation in human tissues: Simulation and sensitivity analysis," in *Proc. IEEE International Conference on Robotics and Automation*, vol. 2, 2003, pp. 1793–1799.
- [36] S. P. DiMaio and S. E. Salcudean, "Needle insertion modeling and simulation," *IEEE Trans. Robot. Autom. (Special Issue on Medical Robotics)*, vol. 19, no. 5, pp. 864–875, Oct. 2003.
- [37] S. P. DiMaio, "Modeling, simulation, and planning of needle motion in soft tissues," Ph.D. dissertation, Univ. Br. Columbia, Vancouver, BC, Canada, 2003.
- [38] D. L. James and D. K. Pai, "ArtDefo: Accurate real time deformable objects," *Computer Graphics—Proc. SIGGRAPH'99*, pp. 65–72, 1999.
- [39] S. Cotin, H. Delingette, and N. Ayache, "Real-time elastic deformations of soft tissues for surgery simulation," *IEEE Trans. Vis. Comput. Graphics*, vol. 5, no. 1, pp. 62–73, Jan.–Mar. 1999.

- [40] A. Hagemann, K. Rohr, H. S. Stiehl, U. Spetzger, and J. M. Gilsbach, "Nonrigid matching of tomographic images based on a biomechanical model of the human head," *Medical Imaging—Image Processing*, pp. 583–592, 1999.
- [41] C. Cuvelier, A. Segal, and A. A. van Steenhoven, *Finite Element Methods and Navier-Stokes Equations*. Dordrecht, The Netherlands: D. Reidel, 1986.
- [42] M. Bro-Nielsen, "Finite element modeling in surgery simulation," *Proc. IEEE*, vol. 86, no. 3, pp. 490–503, Mar. 1998.
- [43] S. P. DiMaio and S. E. Salcudean, "Simulated interactive needle insertion," in *Proc. 10th Symp. Haptic Interfaces for Virtual Environment and Teleoperator Systems*, Mar. 2002, pp. 344–351.
- [44] G. H. Golub and C. F. V. Loan, *Matrix Computations*, 3rd ed. Baltimore, MD: Johns Hopkins Univ. Press, 1996.
- [45] Y. Zhuang, "Real-time simulation of physically realistic global deformations," Ph.D. dissertation, Univ. California at Berkeley, Berkeley, Fall 2000.
- [46] Y. Zhuang and J. Canny, "Haptic interaction with global deformations," in *Proc. IEEE Int. Conf. Robotics and Automation*, Apr. 2000, pp. 2428–2433.
- [47] S. P. DiMaio and S. E. Salcudean, "Needle steering and model-based trajectory planning," in *Proc. Medical Image Computing and Computer Aided Intervention (MICCAI)*, 2003, pp. 33–40.
- [48] ———, "Needle steering and motion planning in soft tissues," *IEEE Trans. Biomed. Eng.*, vol. 52, no. 6, pp. 965–974, Jun. 2005.
- [49] M. R. Sirouspour, S. P. DiMaio, S. E. Salcudean, P. Abolmaesumi, and C. Jones, "Haptic interface control—Design issues and experiments with a planar device," in *Proc. IEEE Int. Conf. Robotics and Automation*, Apr. 2000, pp. 789–794.
- [50] H. Nienhuys and A. F. van der Stappen. (2003) Interactive Needle Insertions in 3-D Nonlinear Material. Inst. Inf. Computing Sci., Utrecht Univ., Utrecht, The Netherlands. [Online]. Available: [www.cs.uu.nl/Tech. Rep. UU-CS-2003-019](http://www.cs.uu.nl/Tech. Rep. UU-CS-2003-019)
- [51] D. L. James, "Multiresolution Green's Function methods for interactive simulation of large-scale elastostatic objects and other physical systems in equilibrium," Ph.D. dissertation, Inst. Appl. Math., Univ. Br. Columbia, Vancouver, BC, Canada, 2001.



**Simon P. DiMaio** (S'98–M'03) received the B.Sc. degree in electrical engineering from the University of Cape Town, Cape Town, South Africa, in 1995. He received the M.A.Sc. and Ph.D. degrees in electrical and computer engineering from the University of British Columbia, Vancouver, BC, Canada, in 1998 and 2003, respectively.

He is currently with the Surgical Planning Laboratory at the Brigham and Women's Hospital, Harvard Medical School, Boston, MA. His research interests include real-time control of dynamic systems, image-guided surgical systems, haptics, medical simulation, and the modeling of physical systems.



**Septimiu (Tim) E. Salcudean** (S'78–M'79–SM'03–F'05) received the B.Eng. and M.Eng. degrees from McGill University, Montreal, QC, Canada, and the Ph.D. degree from the University of California at Berkeley, Berkeley, all in electrical engineering.

From 1986 to 1989, he was a Research Staff Member in the robotics group at the IBM T.J. Watson Research Center. He then joined the Department of Electrical and Computer Engineering at the University of British Columbia, Vancouver, BC, Canada, where he is now a Professor and holds a

Canada Research Chair. He spent one year at ONERA in Toulouse, France, in 1996–1997, where he held a Killam Research Fellowship. He is interested in haptic interfaces, teleoperation, virtual environments and the identification of mechanical properties of tissue using ultrasound elastography. He is pursuing applications to medical diagnosis and interventions.

Prof. Salcudean has been a co-organizer of several symposia on haptic interfaces and a Technical and Senior Editor of the *IEEE TRANSACTIONS ON ROBOTICS AND AUTOMATION*. He is a Fellow of the Canadian Academy of Engineering.